11th International Conference on Ground Penetrating Radar, June 19-22, 2006, Columbus Ohio, USA

Visualization of active faulting using 3-D GPR data recorded across the Alpine Fault, New Zealand

Alastair McClymont*, Rita Streich, Björn Heincke, Alan Green
Institute of Geophysics
Swiss Federal Institute of Technology
ETH Hoenggerberg, 8093 Zurich, Switzerland
*amcclymont@aug.ig.erdw.ethz.ch

David Nobes
Department of Geological Sciences
University of Canterbury
P.O. Box 4800, Christchurch, New Zealand

Abstract – Three-dimensional (3-D) GPR data were acquired across braided river sediments cut by the Alpine Fault at Calf Paddock, New Zealand. We used 100 MHz antennas to obtain images of the subsurface to a depth of 15 m. Cross-sections and depth-converted time slices selected from the migrated data volume show both the structural contrast generated by recent offsets of the fault and the variable orientation of the dipping structures within the braided river deposits. A trace-correlation technique is used to generate dip and dip-direction attribute maps that allow us to visualize the 3-D orientation of the dipping structures. The attribute maps reveal at least 3 different reflection patterns and the presence of minor faulting away from the main fault. A correlation-based migration technique applied to a 2-D GPR profile resulted in the successful identification of the main fault and subsidiary faults at distances up to 50 m from the main fault.

***Keywords* – 3-D GPR; Alpine Fault; active faults; braided river deposits; attribute maps; correlation-based migration.**

I. INTRODUCTION

The Alpine Fault is one of the world's major continental transform zones. It extends for at least 850 km across the South Island of New Zealand (Fig. 1a). The fault accommodates relative motion between the Pacific and Australian Plates but despite average plate-convergence rates of 30-40 mm/yr, has not ruptured during the ~ 150 years of European settlement in New Zealand [1]. Paleoseismic investigations of the fault are ongoing in an attempt to mitigate the effects of future hazards (e.g. [2], [3], [4]).

At Calf Paddock, the Alpine Fault has displaced a sequence of river terraces on the bank of the Maruia River. Surface mapping of the offset terraces and channels has revealed a complicated but poorly understood paleoeseismic history at this site [5], [6]. We recorded 2-D and 3-D GPR data across the surface escarpment of the fault at Calf Paddock to elucidate the subsurface architecture of the late Quaternary river gravels and identify features displaced by the fault. To improve our interpretation we have employed 2 different trace-attribute techniques that allow us to visualize the orientation of dipping reflectors within the braided river deposits and to analyze the data for near-vertical fault structures.

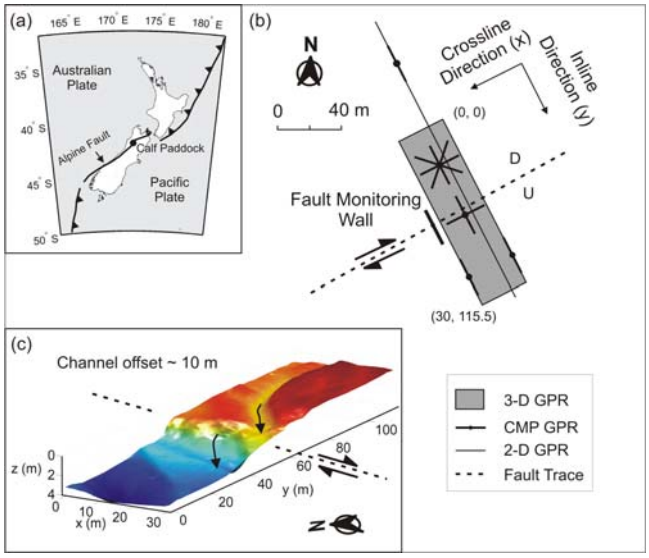

Figure 1. (a) Survey location on the South Island of New Zealand. (b) Survey geometry at Calf Paddock. Symbols D and U indicate the locally downthrown and upthrown sides of the Alpine Fault, respectively. (c) Topographic surface of the 3-D GPR survey area exemplifying recent vertical and horizontal displacement. The trough of an abandoned stream channel is indicated with black arrows. Coordinates (x, y) for the corners of the 3-D survey are in meters.

II. ACQUISITION AND PROCESSING

We acquired our data at Calf Paddock using a semi-automated acquisition system that consists of a standard PulseEkko GPR unit linked to a self-tracking laser theodolite with automatic target recognition capabilities [7]. For the 3-D survey, 100 MHz antennas were used to record radar traces at intervals of approximately 0.25 m along 115- m-long lines separated by about 0.5 m and oriented perpendicular to the scarp of the fault (Fig. 1b).

After applying a standard dewow filter, coordinates recorded by the theodolite were assigned to each trace. All traces were aligned to a common time-zero by cross-correlating airwave arrivals. The irregularly spaced traces were then interpolated using a Delaunay triangulation method on to a regularly spaced grid with inline and

crossline spacings of 0.25 m and 0.5 m, respectively. The gridded 3-D dataset provides a total of 28304 stacked traces over an 30 x 115 m area. The surface elevations clearly illustrate the location of the fault trace and the vertical and lateral offsets of the terrace surface; the terrace surface is vertically offset by ~ 1.5 m (downthrown to the northwest) and an abandoned stream channel on the terrace surface is dextrally displaced by ~ 10 m (Fig. 1c). These observations support those reported from a recent geomorphic investigation of the site [6].

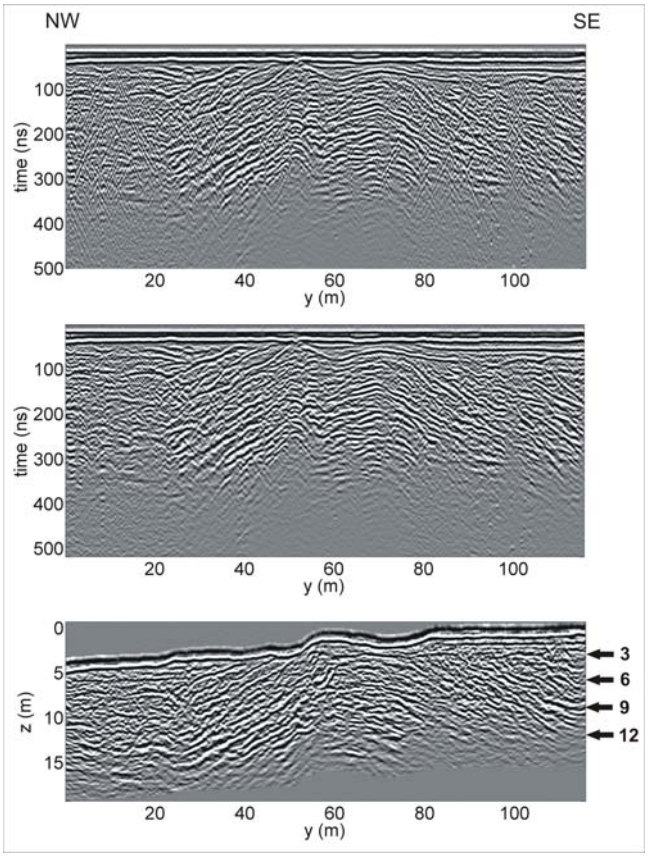

Figure 2. (a) Unmigrated inline GPR cross-section at x = 15 m. (b) The same inline cross-section after 3-D *f-k* filtering has removed the steeply dipping dispersive diffractions, the apices of which, originate at times earlier than the first observable reflections. (c) The same inline cross-section after 3-D topographic migration and depth conversion. The black arrows denote the intersections of the depth slices shown in Fig. 3. The 3 – 6 m depth interval was used for our trace correlation analysis (Fig. 4).

To extract maximum depth information the traces were scaled by the inverse of their amplitude envelopes [8]. The scaled and bandpass filtered data reveal coherent reflections to at least 300 ns (Fig. 2a). Multiple common-midpoint profiles (CMPs) were recorded at different sites to estimate the subsurface velocities within the survey area (Fig. 1b). A strongly dispersive groundwave observed on the CMPs is attributed to a thin low-velocity soil layer in the near surface that acts as a waveguide [9], [10]. Diffractions originating from boulders within this layer exhibit the same dispersive character in the common offset data. They cannot be collapsed using standard migration techniques (Fig. 2a), but they are well separated from the more shallow dipping reflections in the frequency-wavenumber (*f-k*) domain and were effectively removed by three-dimensional *f-k* filtering (Fig. 2b). Finally, the data were migrated using a Kirchhoff-based algorithm that accounts for the significant topography of the survey area [11]. After testing a range of velocities within the limits observed from the CMPs, the most coherent migrated images were obtained using a velocity of 0.08 m/ns (Fig. 2c).

III. ATTRIBUTE ANALYSIS

From the migrated inline cross-sections and depth converted time slices, we observed near-planar reflections with variable dips and dip-directions (Fig. 2, 3). To visualize the 3-D orientations of the subsurface structures within the migrated and depth-converted volume, we employed a trace-correlation algorithm. Each trace was cross-correlated with 4 adjacent traces (2 on each inline and 2 on each crossline) over a 6 - 9 m depth interval. The output lags from the 4 cross-correlations at each trace location were used to calculate the dip and dip-direction of the planar reflections.

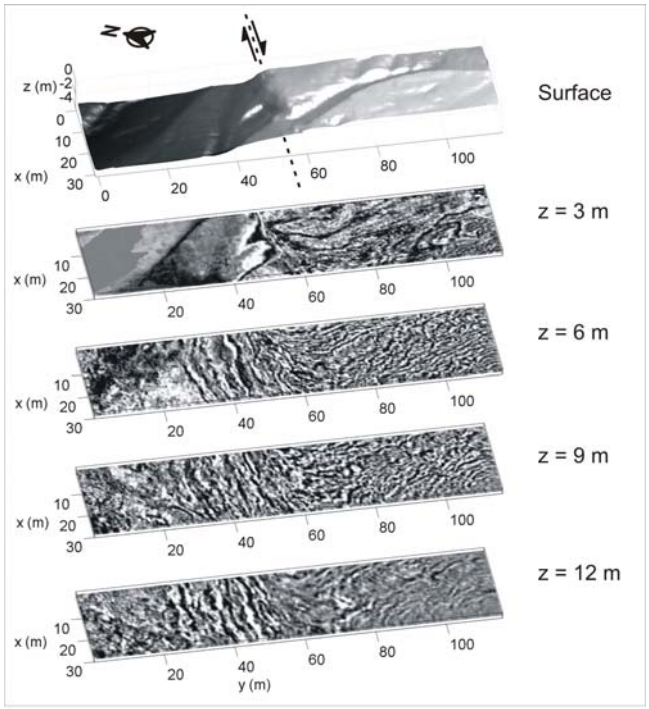

Figure 3. (a) Illuminated perspective view of topography over the 3-D GPR volume. The dashed line and arrows indicate the fault's mapped location and sense of motion. (b) to (e) Depth converted time slices extracted from the migrated GPR volume at z = 3 m, 6 m, 9 m and 12 m.

Figs. 4a and 4b show the resultant dip-directions and dips. We have omitted correlation attributes at locations where the trace is poorly correlated with neighboring traces. The fault zone is characterized by largely uncorrelated traces giving rise to the absence of attribute values over a 10 m wide zone (defined by dashed lines in Fig. 4). Collectively, the plots of dip-direction and dip reveal 3 reflection patterns: **1**) a package of near horizontal planar reflections between the northwestern end of the survey and y ~ 25 m, **2**) a package of northwest-dipping planar reflections (dip-direction azimuth of ~ 320°, perpendicular to the strike of the fault) that extend between y ~ 25 m and the northwestern side of the fault zone and **3**) a package of reflections that extend between the southeastern side of the fault zone and the southeastern edge of the survey that exhibits dip-direction azimuths that vary between 190º and 250º (Fig. 4a and b). Whereas patterns **2** and **3** are clearly discontinuous across the fault, a gradual increase in dip angle between patterns **1** and **2** from effectively horizontal to ~ 15º suggests some continuity in structure between the two (Fig. 4b). Superimposed on pattern **2** are 2 thin bands that have relatively steep (> 20°) dips (indicated by arrows and denoted **A** and **B** on Fig. 4b). These may result from small offsets on the dipping reflectors caused by subsidiary faults.

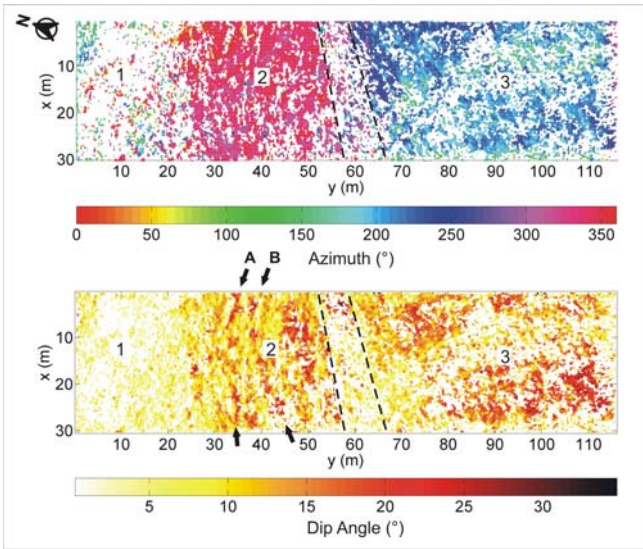

Figure 4. (a) Dip-direction attribute map resulting from cross-correlation of traces between 6 m and 9 m depth. (b) Corresponding dip attribute map. Numbers denote interpreted reflection patterns. Letters and arrows identify interpreted subsidiary fault strands.

Semblance and other coherency-based techniques are widely employed to identify stacking velocities in seismic reflection data [12]. As is common in unmigrated common-offset GPR data, our data set is rich in diffraction hyperbolas originating from point scatterers (Fig. 2a). Coherency-based migration algorithms provide a means to determine subsurface velocities in GPR data. Conversely, if the subsurface velocity is known they can be used to locate point diffractors or edges that may otherwise be obscured by higher amplitude specular reflections. We used a correlation-based migration (CBM) algorithm for GPR data, originally developed to locate near-vertical fractures within crystalline rocks [13], to resolve near-vertical fault structures in the Calf Paddock data.

We applied the CBM method to a long 2-D profile coincident with the x = 10 m cross-section in the 3-D survey (Fig. 1b). As with the 3-D data, the profile data were amplitude scaled and bandpass filtered. However, *f-k* filtering was not applied to the 2-D profile because we wanted to preserve all steeply dipping diffraction tails. The CBM calculates coherency values along migration templates at each subsurface point. To ensure that the entire GPR wavelet is considered in the correlation process, the coherency template is set to cover a finite time interval about each migration template that is equal to the inverse of the lowest dominant signal frequency [13]. Relatively high coherency values in the CBM section of Fig. 5a define at least 3 near-vertical linear features. These are accentuated by removing pixels with coherency values < 2.5 x 10^{-4} (Fig. 5b). In an attempt to objectively enhance these features, we employed a morphology process commonly used in digital image processing [13]. Each data point shown in Fig. 5b is treated as a binary pixel that is either active (black) or inactive (white). Initially, a dilation process activates pixels adjacent to each active pixel. Subsequently, an erosion process removes active pixels from the borders of each cluster of active pixels. The combination of processes effectively closes gaps within clouds of active pixels (Fig. 5c). Finally, we focus our analysis on the larger clusters by removing all clusters comprising less than 20 active pixels (Fig. 5d).

To aid our interpretation, we have plotted the processed CBM data over the conventionally migrated GPR cross-section in Fig. 6. The high coherency values defining lineations **C**, **B** and **D** in Fig. 6 are interpreted to result from offsets on near-vertical faults. The surface extrapolation of lineation **D** coincides with the mapped Alpine Fault. As predicted from our trace correlation technique (Fig. 4b), these 3 lineations to the northwest of **D** are likely the result of subsidiary faulting. Lineation **B** parallels **D** and appears to result from a minor displacement of the dipping reflections northwest of the main fault. The location of lineation **B** is consistent with the location of fault strand **B** identified on the dip-attribute map (Fig. 4b). Lineation **C** occurs where the reflections appear to change abrubtly orientation from northwest dipping to effectively horizontal. This transition is also observed on the dip-attribute map between patterns **1** and **2** (Fig. 4b). The location of subsidiary fault

strand **A** identified on Fig. 4b is not obvious on the CBM plot (Fig. 6). However, the extrapolation of a short lineation of high coherency values (**A?** in Fig. 6) matches the location of subsidiary fault strand **A** in Fig. 4b.

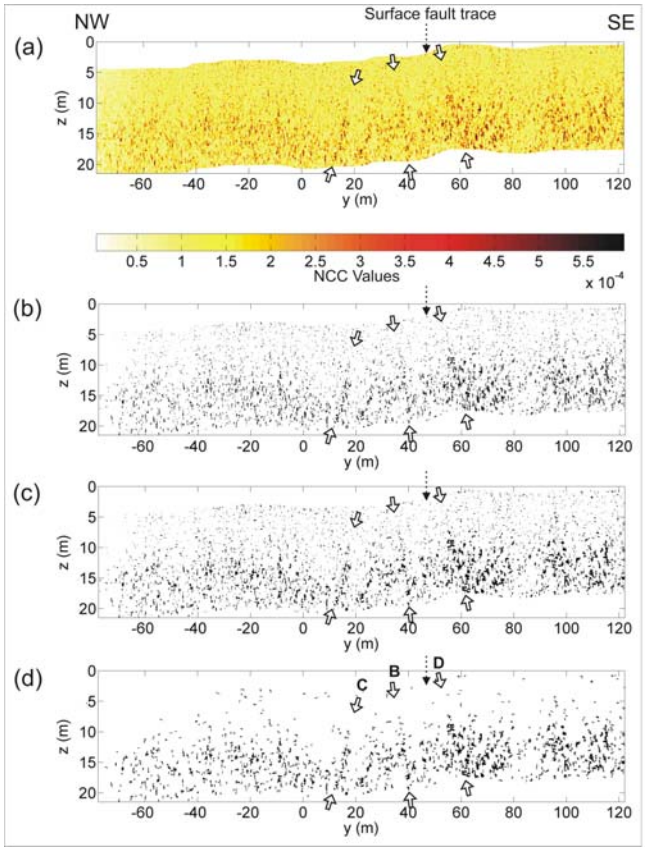

Figure 5. Results of CBM and subsequent digital image processing of the long 2-D GPR line at x = 10 m. Open arrows indicate prominent lineations (a) Coherency values for all data points (pixels) after CBM. Three prominent linear features are indicated by the open arrows. (b) Subset of data pixels with coherencies ≥ 2.5 × 10^{-4}. (c) The resulting pixels after application of 'closing' morphology procedure. (d) After removal of small clusters (< 20 pixels). Lineations C, B and D are explained in Fig. 6.

IIII. CONCLUSIONS

Migrated 3-D GPR data provide clear and interpretable images of the complex subsurface environment at Calf Paddock, where braided river sediments have been deposited across the active Alpine Fault. Cross-sections and depth-converted time slices extracted from the topographically-migrated GPR volume reveal packages of reflections with different orientations. A trace correlation technique allows the complex 3-D geometry of the dipping reflectors to be visualized in the form of dip and dip-direction attribute maps. The Alpine Fault is distinguished by an abrupt change in dip-direction of reflections from ~ 320° on the northwestern side of the fault to between 190º and 250º on the southeastern side. Thin bands of steeply dipping reflections on the northwest side of the fault suggest the presence of subsidiary faults. A CBM technique applied to a 2-D profile successfully identified the location of the main fault and provides evidence for at least 2 subsidiary fault strands. The identification of subsidiary faulting at Calf Paddock implies that near surface deformation related to recent surface rupturing events extends across a margin up to 50 m from the main fault. Future work will attempt to reconcile the subsurface observations with the existing interpretation of the paleoseismic history derived from surface observations.

ACKNOWLEDGMENTS

We greatly appreciate the contributions of Jens Tronicke, Heinrich Horstmeyer and other members of the ETH-University of Canterbury field crew. This project was supported by grants from the Swiss National Science Foundation and ETH-Zurich.

REFERENCES

[1] Wells, A., Yetton, M. D., Duncan, R. P., Stewart, G. H., Prehistoric dates of the most recent Alpine fault earthquakes, New Zealand, *Geology*, vol. 27, 995-998 (1999).

[2] Yetton, M. D., Progress in understanding the paleoseismicity of the central and northern Alpine Fault, Westland, New Zealand, *New Zealand Journal of Geology and Geophysics*, vol. 41, 475-483 (1998).

[3] Bull, W. B., Prehistorical earthquakes on the Alpine Fault, New Zealand, *Journal of Geophysical Research*, vol. 101, 6037-6050 (1996).

[4] Cooper, A. F., Norris, R. J., Displacement on the Alpine Fault at Haast River, South Westland, New Zealand, *New Zealand Journal of Geology and Geophysics*, vol. 38, 509-514 (1995).

[5] Wellman, H. W., The Alpine Fault in detail: river terrace displacement, Maruia River, *New Zealand Journal of Science and Technology*, B33, 409-414 (1952).

[6] Yetton, M. D., Paleoseismic investigation of the north and west Wairau sections of the Alpine Fault, South Island, New Zealand, New Zealand Earthquake Commission Research Report No. 99/353 (2002).

[7] Lehmann, F., Green, A. G., Semi-automated georadar data acquisition in three dimensions, *Geophysics*, vol. 64, 719-731 (1999).

[8] Gross, R., Green, A. G., Horstmeyer, H., Location and geometry of the Wellington Fault (New Zealand) defined by detailed three-dimensional georadar data, *Journal of Geophysical Research*, vol. 109, Art. No. B05401 (2004).

[9] Streich, R., van der Kruk, J., Green, A. G., Three-dimensional multicomponent georadar imaging of sedimentary structures, *Near Surface Geophysics*, (in press).

[10] van der Kruk, J., Streich, R., Green, A. G., Properties of surface waveguides derived from separate and joint inversion of dispersive TE and TM GPR data, *Geophysics* (in press).

[11] Lehmann, F., Green, A. G., Topographic migration of georadar data: implications for acquisition and processing, *Geophysics*, vol. 65, 836-848 (2000).

[12] Neidell, N., Taner, M., Semblance and other coherency measures for multichannel data, *Geophysics*, vol. 36, 482-497 (1971).

[13] Heincke, B., Green, A. G., v. d. Kruk, J., Willenberg, H., Semblance-based topographic migration (SBTM): a method for identifying fracture zones in 3-D georadar data, *Near Surface Geophysics*, (in press).

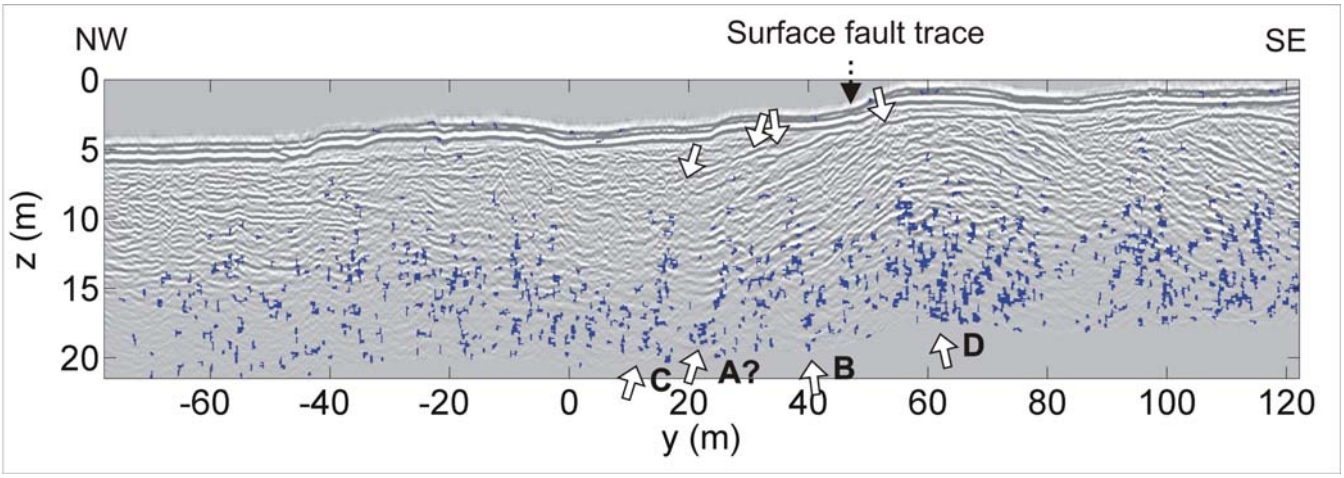

Figure 6. The processed coherency data pixels (red) plotted over the conventionally migrated section (grayscale). At least 3 prominent lineations attributable to fault structures are visible (C, B and D). A combined interpretation of the coherency values and the dip attribute map displayed in Fig. 4b suggests the presence of a 4th lineation (A?)